

Site-Controlled Telecom Single-Photon Emitters in Atomically-thin MoTe₂

Huan Zhao

Center for Integrated Nanotechnologies, Materials Physics and Application Division, Los Alamos National Laboratory

Micahel Pettes

Center for Integrated Nanotechnologies, Materials Physics and Application Division, Los Alamos National Laboratory

Yu Zheng

Center for Integrated Nanotechnologies, Materials Physics and Application Division, Los Alamos National Laboratory

Han Htoon (✉ htoon@lanl.gov)

Center for Integrated Nanotechnologies, Materials Physics and Application Division, Los Alamos National Laboratory <https://orcid.org/0000-0003-3696-2896>

Letter

Keywords: quantum emitters (QEs), MoTe₂, quantum communication, transduction research

Posted Date: July 23rd, 2021

DOI: <https://doi.org/10.21203/rs.3.rs-452814/v2>

License:   This work is licensed under a Creative Commons Attribution 4.0 International License.

[Read Full License](#)

Version of Record: A version of this preprint was published at Nature Communications on November 19th, 2021. See the published version at <https://doi.org/10.1038/s41467-021-27033-w>.

Abstract

Quantum emitters (QEs) in two-dimensional transition metal dichalcogenides (2D TMDCs) have advanced to the forefront of quantum communication and transduction research¹. To date, QEs capable of operating in O-C telecommunication bands have not been demonstrated in TMDCs.²⁻⁵ Here we report a deterministic creation of such telecom QEs emitting over the 1080 to 1550 nm wavelength range via coupling of 2D molybdenum ditelluride (MoTe₂) to strain inducing nano-pillar arrays.^{6, 7} Our Hanbury Brown and Twiss experiment conducted at 10 K reveals clear photon antibunching with 90% single photon purity. The photon antibunching can be observed up to liquid nitrogen temperature (77 K). Polarization analysis further reveals that while some QEs display cross-linearly polarized doublets with ~1 meV splitting resulting from the strain induced anisotropic exchange interaction, valley degeneracy is preserved in other QEs. Valley Zeeman splitting as well as restoring of valley symmetry in cross-polarized doublets are observed under 8T magnetic field.

Main Text

Quantum emitters (QEs) that emit one photon at a time are key building blocks for numerous quantum technology protocols such as quantum communications, quantum information processing, and quantum key distribution.⁸⁻¹⁰ In particular, QEs operating in the telecom bands (1.25–1.55 μm) are highly desired for implementation of quantum technologies through existing fiber-based optical communication networks. Currently, telecom-compatible QEs have been demonstrated in various III-V semiconductor quantum dots^{11, 12} and recently in functionalized carbon nanotubes.^{5, 13} However, several challenges such as accurate site positioning and efficient polarization control still remain for these QEs. Over the past decade, two-dimensional (2D) semiconductors have emerged as a novel platform for both fundamental research and technological applications. Leveraged by the unique membrane-like geometry, 2D semiconductors are promising for QEs as they offer high photon extraction efficiency, easy coupling to external fields, and convenient integration with photonic circuits. In addition, strain engineering can be readily applied to accurately position the emission sites.^{6, 7, 14} Most importantly, 2D transition metal dichalcogenides (TMDCs) have a valley degree of freedom that can be manipulated and accessed through circularly polarized excitonic optical transitions and efficiently tuned via a magnetic field,^{15, 16} bringing new quantum functionalities to embedded QEs. Recently, 2D QEs have been demonstrated in WSe₂²⁻⁵ and hexagonal boron nitride,^{17, 18} covering a broad emission spectrum range from ~500–800 nm. However, Single-Photon emitter (SPE) in the most desirable spectral range – the telecom bands – has never been explored in 2D systems. While most 2D semiconductors have inherent electronic band structures that limit the operating wavelength to the visible range, alpha-phase 2H-MoTe₂ has a layer-dependent bandgap in the NIR regime, holding promise for telecom-compatible single photon emission.

We demonstrate the first observation of telecom single-photon emission in MoTe₂ mono- and few-layers. We transferred mechanically exfoliated MoTe₂ thin flakes onto nanopillar arrays to introduce strain-induced exciton localization potential (see Methods and **Supplementary Section S1**). We observed QEs in

both monolayer and relatively thick (>10 layers) MoTe₂ flakes. **Figure 1a** is an optical image of a MoTe₂ monolayer on nanopillar arrays. The corresponding wide-field photoluminescence (PL) image, **Figure 1b**, shows significantly brighter PL emission in strained region. Unstrained monolayer MoTe₂ features two dominant emission peaks at cryogenic temperature: exciton (X⁰) emission at around 1050 nm and trion (X[±]) emission at around 1070 nm (**Figure 1c**).^{19,20} With localized strain, a series of narrow PL peaks covering a broad spectral range of 1080 – 1150 nm emerges from the lower energy side of the spectrum (**Figure s3**). We attribute these PL peaks to the localized exciton states arising from strain induced hybridization of dark exciton and the defect states.^{21,22} The linewidths of the QE PL emission range from a few meV to sub-meV at 10 K temperature, which are nearly an order of magnitude narrower than the linewidths of the 2D exciton PL peaks (~ 10 meV). The narrow near-band-edge emission lines are also frequently observed in 2–4 layered samples but are not seen in much thicker flakes. **Figure 1d** shows a typical narrow PL peaks from a QE that displays a linewidth (full width at half maximum, FWHM) of 920 meV. The peak is accompanied by a weak shoulder peak at ~ 2.5 meV higher energy side. Both the width and shape of this PL peak remain essentially unchanged over nearly 3 order of magnitude change in pump power. The PL intensity also vary linearly with pump power and only shows a weak saturation at powers >300 nW (**figure 1e**).

To access the single photon emission characteristics of the QEs, we performed time-tagged, time-correlated single photon counting and Hanbury Brown-Twiss (HBT) experiments. The PL intensity time trace, PL decay curve and second-order correlation at zero time delay, or $g^2(0)$, was extracted from the photon stream. **Figure 2a** displays the PL spectrum of a strain-induced localized emitter, of which the measurement results are presented in **Figure 2b-d**. The PL decay curve (**Figure 2b**) shows a near-perfect single-exponential decay with a lifetime $\tau = 22.2 \pm 0.1$ ns that is four orders of magnitude longer than that in pristine MoTe₂ (~2 ps).²³ This long lifetime provides a clear indication that localization of the exciton in a strain induced potential trap suppress non-radiative recombination through defects states that dominate the decay of 2D band-edge excitons.²³

Quantum-dot-like solid-state QEs typically have instability issues such as photon bleaching, blinking, and spectral diffusion, which hinders applications.²⁴ We monitored the time-dependent PL emission under both pulse and CW laser excitation (**Figure 2b, inset, Figure s4a**), revealing a stable emission at average count rates of 1.2 kHz for pulse (9 kHz for CW) excitation without detectable photo-bleaching or blinking over the timescales presented. A time series of PL spectra also show no spectral diffusion (**Figure s6**). **Figure 2c and 2d** present the photon correlation under pulsed [$g^2(0) = 0.058 \pm 0.003$] and CW [$g^2(0) = 0.181 \pm 0.030$] excitation, respectively. Both values are well below the photon antibunching threshold of $g^2(0) = 0.5$, which unequivocally reveals that the strain-induced MoTe₂ localized emitter is indeed a QE. HBT experiment conducted on a different emitter at 40 K and 77 K have further evinced that the single photon emission behavior can survive up to liquid nitrogen temperature, although the PL emission decreases significantly (**Figure s5**). Normalizing the measured count rates of QE of Figure 2 with the overall collection efficiency of our microPL system at 1108 nm (0.035%) (**Supplementary Section S3**), we

estimate the corrected emission rate of the QE to be 3.4 MHz for pulse (25.6 MHz for CW) excitation. Assuming that an exciton is localized into the QE in every excitation cycle, we can further deduce the radiative recombination efficiency of the QE to be $\sim 7\%$ from the ratio between the corrected emission rate under pulse excitation and the 48.5 MHz pulse excitation rate.^{14, 25, 26} This low efficiency could result from thermal hopping of excitons out of the shallow trapping potential. The efficiency increases significantly when the QE is isolated in energy from the band-edge (see below).

Obtaining telecom-compatible QEs that emit at around 1.3 μm (O-band, “original band”) and 1.55 μm (C-band, “conventional band”) are required for fiber-based quantum communications. When increasing the MoTe_2 layer numbers from monolayer to bulk, the bandgap of MoTe_2 decreases from 1.18 eV (1050 nm) to 0.95 eV (1300 nm) monotonically.²⁰ The PL intensity also decreases orders of magnitude due to a direct-to-indirect bandgap transition commonly observed in 2D TMDCs. In our experiment, we observe bright localized telecom-band emissions from strained few-layer MoTe_2 although we have occasionally found such emissions in mono- and bilayer samples (**Supplementary Section S6- S8**). **Figure 3a** and **Figure s7a,b** present PL spectra of telecom-wavelength emitters. We typically observe such highly red-shifted bright emissions spanning 1.25–1.55 μm , covering the full telecom window. **Figure s8** shows that such QEs, emitting at wavelength longer than 1300 nm are created in a 5-6 layer thick MoTe_2 at almost all the nano-pillar sites. In contrast to near-band-edge QEs, these are characterized by relatively broad linewidths (FWHM 7~30 meV). **Figure 3b** is the PL spectrum of a telecom QE, of which PL dynamics and photon correlation results are presented in **Figure 3c-3f**, respectively. We observed an initial PL decay with a lifetime of 163 ± 3 ns, followed by an ultra-long lifetime of 1.13 ± 0.01 ms. This ultra-long lifetime is attributed to the dominant PL peak at lower energy, confirmed by comparing the integrated PL counts from the TRPL curve with the PL counts in spectrum (details given in **Supplementary Section S9**). The measured lifetime is 6 orders of magnitude longer than that of the MoTe_2 band-edge emission and is of 2–3 orders larger than that of the near-band-edge QEs. Based on this long lifetime and the fact that these telecom-QEs are observed more on multilayer thick MoTe_2 , we tentatively attribute the telecom-QEs to indirect excitonic transitions, which are activated by strain induced quantum confinement potentials. **Figure 3d** show that this telecom-QE is also free from blinking or photon bleaching over 5000 s experiment time. The HBT experiment under pulsed excitation for the spectral window shown in **Figure 3b** yield a $g^2(0) = 0.48 \pm 0.03$ (**Figure 3e**). Since this measurement includes contribution from a high-energy shoulder that exhibits shorter PL decay, we employed a time gated $g^{(2)}$ experiment²⁷ (**Supplementary Section S10**), in which only the photons arriving after the decay of the higher energy shoulder (i.e. after 200 ns delay) were analyzed for the $g^{(2)}$ trace. The time gated $g^{(2)}$ in **Figure 3f** shows $g^2(0) = 0.155 \pm 0.009$ clearly proving the antibunching nature of the 1540 nm telecom emitter. Our result is the first ever demonstration of a 2D, telecom C-band QE. HBT experiments of other two QEs emitting at 1340 (O-band) and 1200 nm yielding $g^2(0)$ of 0.28 ± 0.02 and 0.26 ± 0.02 respectively are also shown in **Figure s9**. Using overall collection efficiency of the our micro PL system at 1550 nm (0.31%) (**Supplementary Section S3**) and 303 kHz pulse excitation rate, we can estimate the absolute emission rate and radiative recombination efficiency of the QE of Fig. 3 to be 258 kHz and 85%,

respectively.^{14, 25, 26} The radiative efficiency of the telecom QEs is significantly higher than that of the near-band-edge QEs because the deep trapping potential of the telecom QEs could strongly suppress thermal detrapping of exciton which is believed to be responsible for low radiative efficiency of band edge QEs. This fact is also consistent with the extra-long PL lifetime of the telecom QEs. While this long PL lifetime is not favorable for SPE applications, it can be improved through plasmonic enhancement.¹⁴

To investigate the valley physics of QEs in MoTe₂, we conducted polarization-resolved magneto-PL spectroscopy with a field normal to the sample surface (Faraday geometry). **Figure 4a** presents a helicity-resolved PL of a MoTe₂ QE. The spectra was taken with s + excitation and analyzed for both s + and s – helicities. The valley Zeeman splitting was not observed in the absence of a magnetic field but rose with increasing field, indicating a lifting of valley degeneracy. Using the relation between the energy splitting ΔE and the magnetic field B , $\Delta E = -g\mu_B B$, where μ_B is the Bohr magneton, we extracted a Landé g -factor of -3.61 ± 0.02 for the QE (**Supplementary Section S11**), which is comparable with g -factors reported in other work.²⁸ At zero field, the degree of circular polarization, $P_C = (I_{\sigma^+} - I_{\sigma^-}) / (I_{\sigma^+} + I_{\sigma^-})$ was 13% as a result of the valley-selective-pumping effect. Significant valley polarization was observed with an applied magnetic field, reaching 52% at 8 T, which is more pronounced compared to the 30% polarization reported in magnetic-field induced valley polarization of intrinsic MoTe₂ excitons.²⁸ These results indicate a vanishing fine structure splitting of the QE at zero field, which could be exploited for entangled photon generation through the biexciton/exciton cascade.

We also observed emission pairs in some of the QEs, which were found to be cross-linearly polarized doublets with sizeable zero-field energy splitting (1-3.7 meV) (**Figure 4b** and **Supplementary Section S12**). The two peaks from the doublet have a zero-field splitting of 1.09 meV and reach their maximal PL intensities in opposite linear polarization directions (horizontal/vertical), indicating the presence of fine structure. The observed cross-polarization and zero-field energy splitting have also been reported in III-V quantum dots^{29, 30} and recently in WSe₂ QEs.^{2, 4} Following prior studies, we attribute this fine-structure splitting to hybridization of K and K' valley polarized excitons by an asymmetric potential landscape defined by the localized strain as illustrated in **Figure 4d**. When the magnetic field is strong enough to overcome the anisotropic Coulomb potential (i.e. $\Delta E_{ZS} > \Delta E_0$), the linearly polarized states vanish and circularly polarized states are recovered. This restoration of valley symmetry is achieved in our QE under an 8 T magnetic field (**Figure 4c**).

Methods

Sample Preparation. MoTe₂ flakes were mechanically exfoliated from a flux-grown bulk crystal before they were transferred onto pre-patterned substrates. Thin layers (that is, flakes that look greenish and translucent under an optical microscope) were selected for further optical characterizations. 1-4 layer flakes can be easily distinguished by analyzing the band-edge emission wavelength and PL intensity.²² Flakes thicker than four layers do not have a detectable band-edge emission using mW level pump power. To prepare the strained substrates, a 50 nm Au layer was deposited on top of a Si/SiO₂ substrate to block

silicon emission, followed by the spin-coating of a 50 nm polyvinyl alcohol (PVA) dielectric layer to avoid quenching effects. Then, a ~120 nm polymethyl methacrylate (PMMA) layer was spin-coated on top of the PVA layer and patterned by electron beam lithography into PMMA nanopillar arrays with a 3 mm pitch width. A 90°C vacuum annealing was applied to enhance the contact between the 2D flakes and the nanopillars. Each pillar had a ~100 nm pillar height and a ~150 nm diameter. Note: later we found the PVA spacer layer was not necessary as the ~100 nm PMMA pillars were sufficient to separate the MoTe₂ dots from the gold layer and maintain efficient PL emission.

Optical Characterization. A diagram of our optical measurement setup is presented in **Supplementary Section S13**. Micro-PL measurements of MoTe₂ QEs were performed on a home-built confocal microscope with excitation of either an 850 nm CW Ti:sapphire laser or an 850 nm supercontinuum pulsed laser. The excitation power was typically a few mW. Samples were mounted in a continuous flow cryostat and cooled to 10–13 °K using liquid helium. The emitted light was collected through a 50× infrared objective lens (Olympus, 0.65 NA) and spectrally filtered before entering a 2D InGaAs array detector (NIRvana 640LN, Princeton Instruments). We used 150 and 300 gr/mm gratings to resolve the spectra. For TRPL and HBT experiments, the emission signal was spectrally filtered before coupled into a 50:50 optical fiber beamsplitter, which equivalently split the signal into two beams and sent them into two channels of a superconducting nanowire single-photon detector (Quantum Opus). PL intensity time trace, PL decay curves and $g^2(t)$ traces were obtained from photon detection events recorded by a PicoQuant HydraHarp 400 time-correlated single photon-counting module. We applied a bi-exponential decay model to determine the CW $g^2(0)$ value and error level. For pulsed auto-correlation measurements, $g^2(0)$ was extracted by comparing the integrated photon coincidence counts at the zero-time delay peak with the averaged integrated photon coincidence counts at 30 adjacent peaks. The error level of pulsed $g^2(0)$ was defined by the standard deviation of the integrated photon coincidence counts in the adjacent peaks. For the pulsed $g^2(0)$ measurement of the 1540 nm peak, a time gate of 200 ns was applied to significantly reduce the contribution from the undesired emissions that could not be fully removed by optical filters.

For magneto spectroscopy and polarization-resolved PL measurements, the sample was placed inside the room temperature bore of an 8.5 T liquid-helium cooled superconducting magnet. For linear polarization analysis, the excitation beam was fully depolarized using a laser depolarizer to eliminate the polarization memory effect. A half-wave plate (HWP) was inserted into the collection channel to rotate the polarization direction. A Wollaston prism was placed between the HWP and the InGaAs detector to spatially split the emission into horizontal and vertical components, followed by a depolarizer to avoid effects arising from the linear polarization dependence of the gratings. For circular polarization analysis, a quarter-wave plate (QWP) was inserted into the shared path of the excitation and the emission beams. As a result, the QWP turns the linearly polarized laser into a circularly polarized excitation source and converts the circularly polarized PL signals into linearly polarized beams. A HWP and a Wollaston prism were installed in the collection beam to spatially split the s^+ and s^- emissions into two different areas on the 2D InGaAs array.

Declarations

Acknowledgement

The authors would like to acknowledge the helpful discussion and technical support from Dr. Christopher Lane, Dr. Jianxin Zhu, Dr. Andrew Jones and Mr. John Kevin Scott Baldwin. This work was performed at the Center for Integrated Nanotechnologies, an Office of Science User Facility operated for the U.S. Department of Energy (DOE) Office of Science. Los Alamos National Laboratory (LANL), an affirmative action equal opportunity employer, is managed by Triad National Security, LLC for the U.S. Department of Energy's NNSA, under contract 89233218CNA000001. Deterministic quantum emitter creation capability was developed under the support of DOE BES, QIS Infrastructure Development Program BES LANL22. HZ, YZ and HH acknowledge partial support from Laboratory Directed Research and Development (LDRD) program 20200104DR. HH is also partially supported by Quantum Science Center. MTP is supported by LDRD 20190516ECR. HZ also acknowledge a partial support from LANL Director's Postdoctoral Fellow Award.

Author contributions

HZ and HH conceived the experiment. HZ, under the supervision of HH, primarily developed deterministic QE creation approach, designed and conduct the experiment, analyzed the data and composed the paper. YZ assisted in the experiment. MTP assisted in the design of the nanopillar samples and paper preparation.

Competing financial interests

The authors declare no competing financial interests.

References

1. Atatüre, M., Englund, D., Vamivakas, N., Lee, S.-Y. & Wrachtrup, J. Material platforms for spin-based photonic quantum technologies. *Nat. Rev. Mater.* **3**, 38-51 (2018).
2. Srivastava, A. et al. Optically active quantum dots in monolayer WSe₂. *Nat. Nanotechnol.* **10**, 491 (2015).
3. Koperski, M. et al. Single photon emitters in exfoliated WSe₂ structures. *Nat. Nanotechnology* **10**, 503-506 (2015).
4. He, Y.-M. et al. Single quantum emitters in monolayer semiconductors. *Nat. Nanotechnol.* **10**, 497-502 (2015).
5. Chakraborty, C., Kinnischtzke, L., Goodfellow, K.M., Beams, R. & Vamivakas, A.N. Voltage-controlled quantum light from an atomically thin semiconductor. *Nat. Nanotechnol.* **10**, 507-511 (2015).

6. Palacios-Berraquero, C. et al. Large-scale quantum-emitter arrays in atomically thin semiconductors. *Nat. Comm.* **8**, 1-6 (2017).
7. Branny, A., Kumar, S., Proux, R. & Gerardot, B.D. Deterministic strain-induced arrays of quantum emitters in a two-dimensional semiconductor. *Nat. Comm.* **8**, 1-7 (2017).
8. Lodahl, P., Mahmoodian, S. & Stobbe, S. Interfacing single photons and single quantum dots with photonic nanostructures. *Rev. Mod. Phys.* **87**, 347 (2015).
9. Northup, T. & Blatt, R. Quantum information transfer using photons. *Nature Photonics*. **8**, 356-363 (2014).
10. Knill, E., Laflamme, R. & Milburn, G.J. A scheme for efficient quantum computation with linear optics. *Nature* **409**, 46-52 (2001).
11. Buckley, S., Rivoire, K. & Vučković, J. Engineered quantum dot single-photon sources. *Rep. Prog. Phys.* **75**, 126503 (2012).
12. Miyazawa, T. et al. Single-photon generation in the 1.55- μm optical-fiber band from an InAs/InP quantum dot. *Jpn. J. Appl. Phys.* **44**, L620 (2005).
13. He, X. et al. Tunable room-temperature single-photon emission at telecom wavelengths from sp³ defects in carbon nanotubes. *Nat. Photonics* **11**, 577 (2017).
14. Luo, Y. et al. Deterministic coupling of site-controlled quantum emitters in monolayer WSe₂ to plasmonic nanocavities. *Nat. Nanotechnol.* **13**, 1137-1142 (2018).
15. Xu, X., Yao, W., Xiao, D. & Heinz, T.F. Spin and pseudospins in layered transition metal dichalcogenides. *Nat. Phys.* **10**, 343-350 (2014).
16. Mak, K.F., He, K., Shan, J. & Heinz, T.F. Control of valley polarization in monolayer MoS₂ by optical helicity. *Nat. Nanotechnol.* **7**, 494-498 (2012).
17. Sajid, A., Ford, M.J. & Reimers, J.R. Single-photon emitters in hexagonal boron nitride: a review of progress. *Rep. Prog. Phys.* **83**, 044501 (2020).
18. Tran, T.T., Bray, K., Ford, M.J., Toth, M. & Aharonovich, I. Quantum emission from hexagonal boron nitride monolayers. *Nat. Nanotechnol.* **11**, 37-41 (2016).
19. Koperski, M. et al. Optical properties of atomically thin transition metal dichalcogenides: observations and puzzles. *Nanophotonics* **6**, 1289-1308 (2017).
20. Lezama, I.G. et al. Indirect-to-direct band gap crossover in few-layer MoTe₂. *Nano Lett.* **15**, 2336-2342 (2015).

21. Linhart, L. et al. Localized intervalley defect excitons as single-photon emitters in wse 2. *Phys. Rev. Lett.* **123**, 146401 (2019).
22. Parto, K., Banerjee, K. & Moody, G. in *Frontiers in Optics FW1C. 3* (Optical Society of America, 2020).
23. Chi, Z., Chen, H., Zhao, Q. & Weng, Y.-X. Ultrafast carrier and phonon dynamics in few-layer 2H-MoTe₂. *J. Chem. Phys.* **151**, 114704 (2019).
24. Krishnamurthy, S. et al. PbS/CdS Quantum Dot Room-Temperature Single-Emitter Spectroscopy Reaches the Telecom O and S Bands via an Engineered Stability. *ACS Nano* **15**, 575-587 (2020).
25. Strauf, S. et al. High-frequency single-photon source with polarization control. *Nat. Photonics* **1**, 704-708 (2007).
26. Jeantet, A. et al. Widely tunable single-photon source from a carbon nanotube in the Purcell regime. *Phys. Rev. Lett.* **116**, 247402 (2016).
27. Mangum, B.D., Ghosh, Y., Hollingsworth, J.A. & Htoon, H. Disentangling the effects of clustering and multi-exciton emission in second-order photon correlation experiments. *Opt. Express* **21**, 7419-7426 (2013).
28. Arora, A. et al. Valley Zeeman splitting and valley polarization of neutral and charged excitons in monolayer MoTe₂ at high magnetic fields. *Nano Lett.* **16**, 3624-3629 (2016).
29. Gammon, D., Snow, E., Shanabrook, B., Katzer, D. & Park, D. Fine structure splitting in the optical spectra of single GaAs quantum dots. *Phys. Rev. Lett.* **76**, 3005 (1996).
30. Gammon, D., Snow, E., Shanabrook, B., Katzer, D. & Park, D. Homogeneous linewidths in the optical spectrum of a single gallium arsenide quantum dot. *Science* **273**, 87-90 (1996).

Figures

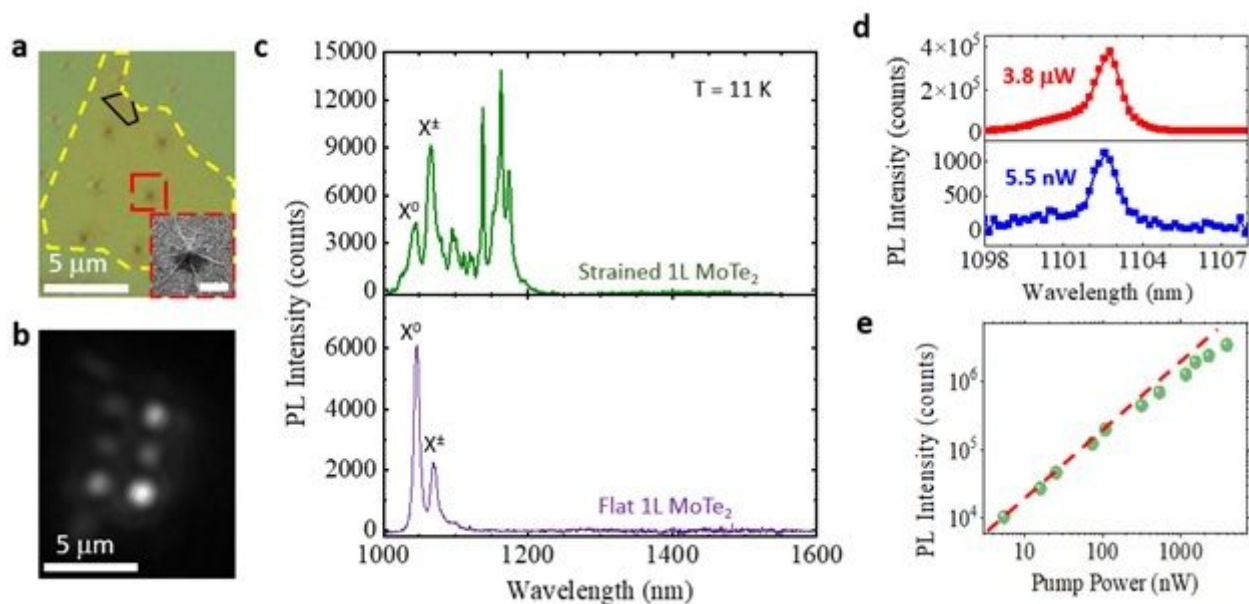


Figure 1

a, Optical image of a monolayer MoTe₂ flake (with a tiny folded bilayer region outlined in black) on nanopillar arrays. The MoTe₂ flake is outlined by yellow dashed lines. Scale bar: 5 μm. Inset: SEM image of a nanopillar coated with monolayer MoTe₂, displaying a tent-shaped strain profile. Scale bar of the inset: 500 nm. b, Wide-field PL image of the same flake. The brighter areas, indicating stronger emission, are consistent with the pillar locations in a. Scale bar: 5 μm. c, PL spectrum of a MoTe₂ monolayer on flat PMMA (lower panel) and the PL spectrum of a MoTe₂ monolayer sitting on a nanopillar (upper panel) acquired at laser excitation power of 0.8 mW and 30s integration time. The MoTe₂ exciton and trion peaks are identified. d, PL spectra of a representative localized MoTe₂ emitter acquired at 3.3 mW and 5.5 nW pump power showing invariant shape and width (920 μeV at FWHM) of the spectral line. e, Pump-power-dependent emission intensity of the PL peak presented in Figure 1d shows near-perfect linear scaling with pump power. The red dash line is to guide the eye. All experimental data were taken at 11 K temperature.

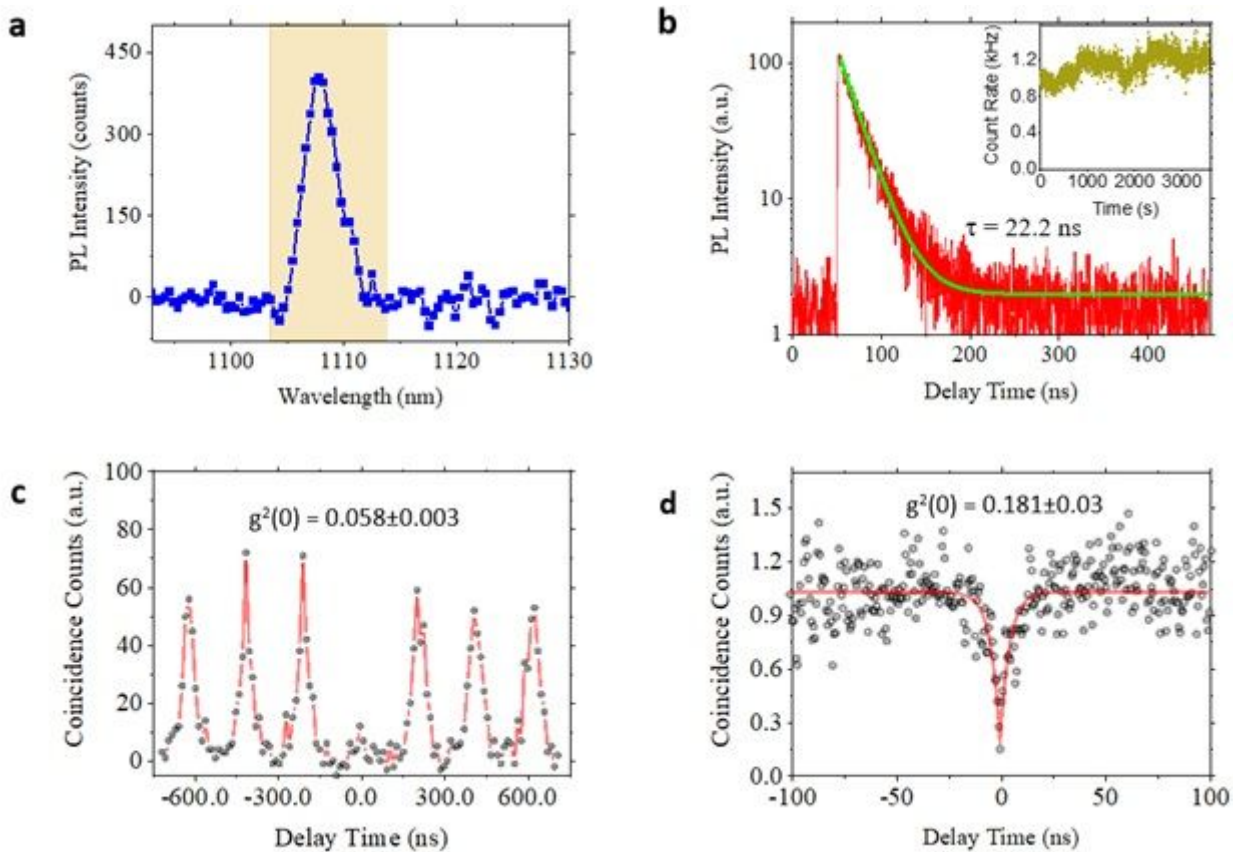


Figure 2

a, PL spectrum of a localized MoTe₂ emitter. The data of b, c, d are taken from this dot with a band pass filter that allows the shadowed region to be detected. b, the PL decay curve (red) and a single exponential decay fit (green) with a $22.2 \pm 0.1 \text{ ns}$ extracted lifetime. Inset plots the PL intensity as a function of experiment time showing stability of the single photon emission rate over 1 hour time. The modulation observed over the long time scale ($\sim 100 \text{ s}$) is mainly due to sample drift relative to the laser excitation spot. c, Second-order correlation measurement under a 850 nm pulse excitation with a 2.1 MHz repetition rate, from which a $g^2(0) = 0.058 \pm 0.003$ is extracted. d, Second-order correlation measurement under a 850 nm CW laser excitation. The red curve is a fit to the data using a bi-exponential decay function. The extracted $g^2(0) = 0.181 \pm 0.030$. All the experimental data were taken at 11 K temperature.

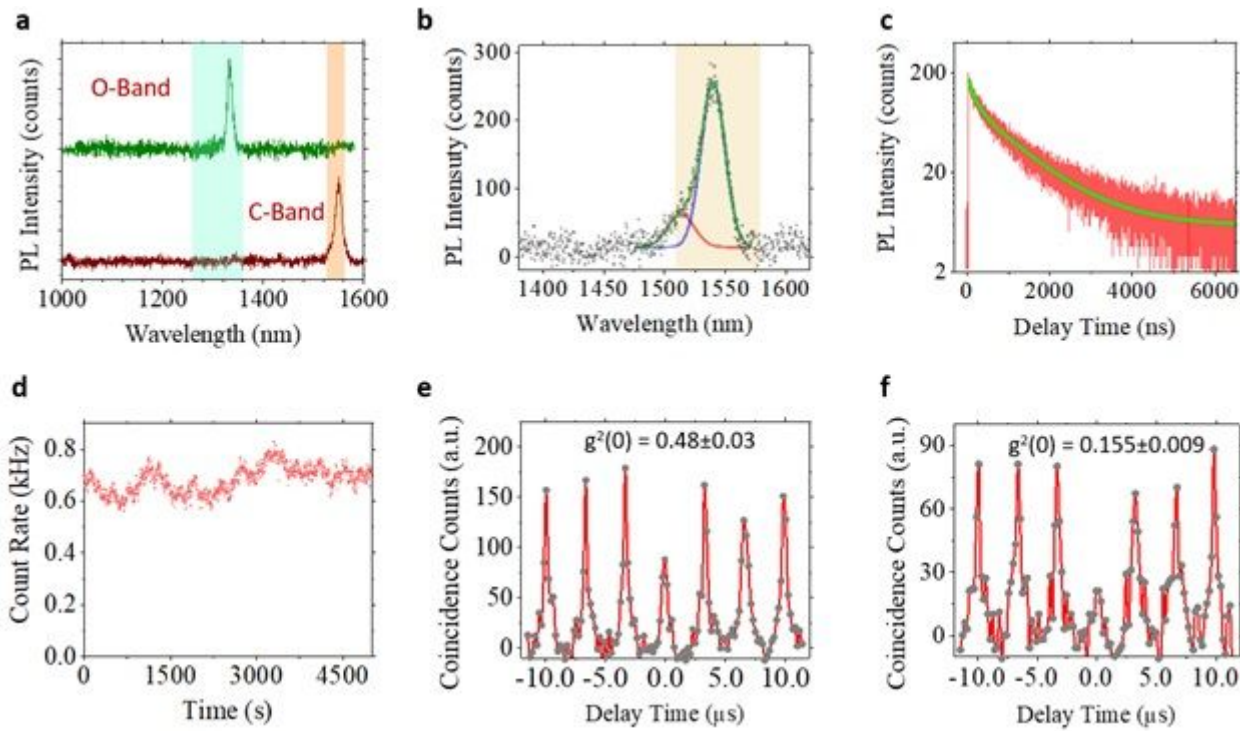


Figure 3

a, “O-band” and “C-band” telecom PL emissions from two multilayer MoTe2 localized emitters. b, MoTe2 quantum dot with a 1540 nm telecom emission peak and a small shoulder peak at 1510 nm. The blue and red lines are Gaussian fits to the 1540 and 1510 nm peaks, respectively. The data of c-f are taken from this dot with a band pass filter that allows the shadowed region to be detected. c, PL decay curve (red) and a bi-exponential decay fit (green) reveal the lifetime of the 1540 nm peak is 1.13 ± 0.01 ms. d, Time-dependent PL counts showing a stable emission over 5000 seconds. Data is recorded every 500 ms. e, Second-order correlation measurement under a 850 nm pulsed excitation with a 330 kHz repetition rate, from which $g^2(0) = 0.48 \pm 0.03$ is extracted. f, Time-gated $g^2(2)$ experiment shows $g^2(0) = 0.155 \pm 0.009$ under a 200 ns time gate. All experimental data were taken at 13 K temperature.

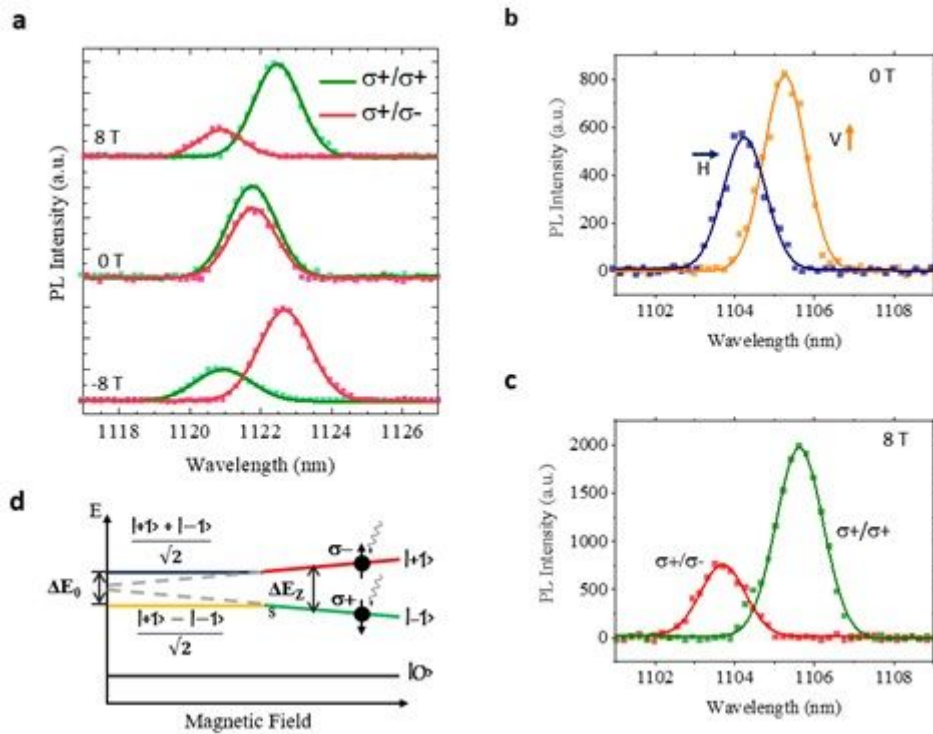


Figure 4

a, Helicity-resolved magneto-PL data of a MoTe2 localized emitter. The emitter was excited using a s+ polarized laser. b, The PL spectrum of a linearly cross-polarized doublet measured at zero field, showing a fine-structure energy splitting of ~ 1.1 meV. H and V denote horizontal and vertical polarization detection directions, respectively. c, Spectrum of the same doublet under an 8 T magnetic field, showing the doublet is converted to a circular cross-polarized pair. The excitation is a s+ polarized laser. The lines in a-c are Gaussian peak fits to the PL data. d, Energy diagram of the doublet as a function of the external magnetic field. The linearly-polarized states are converted into s+ and s- circularly polarized states once the Zeeman energy (ΔE_Z) exceeds the zero-field fine-structure splitting energy (ΔE_0). The ground state is denoted as $|0\rangle$. All experimental data were taken at 11 K temperature.

Supplementary Files

This is a list of supplementary files associated with this preprint. Click to download.

- [MoTe2SPESupplInfoNatPHotonsubmit.docx](#)